

# Designing and Simulating Quantum Imaging Techniques

By

Hania Shahid

Supervisor: Dr. Sabieh Anwar

An abstract of  
A thesis submitted to the Faculty of the  
Syed Babar Ali School of Science and Engineering  
in partial fulfillment of the requirements for the degree of  
Bachelor of Science  
in Physics Department  
2024

## Abstract

### Designing and Simulating Quantum Imaging Techniques By Hania Shahid

This thesis explores the design and simulation of quantum imaging techniques, specifically focusing on ghost imaging and quantum holography. By leveraging the properties of quantum entanglement and interference, this work demonstrates the potential to surpass traditional imaging limitations. Theoretical models are combined with simulation techniques to reconstruct both the amplitude and phase information of objects using quantum phenomena. This study specifically addresses the challenge of validating quantum effects in imaging by bypassing classical light pathways and confirming the reliance on quantum interference. The methodology involves a novel simulation framework that uses phase-shifting holography to extract detailed image properties, which are crucial for applications requiring high precision, such as in medical imaging and microscopy. The results confirm the effectiveness of quantum imaging techniques and provide a foundation for further exploration and practical implementation of these technologies in advanced imaging systems.

# Designing and Simulating Quantum Imaging Techniques

By

Hania Shahid

Supervisor: Dr. Sabieh Anwar

A thesis submitted to the Faculty of the  
Syed Babar Ali School of Science and Engineering  
in partial fulfillment of the requirements for the degree of  
Bachelor of Science  
in Physics Department  
2024

## Acknowledgments

I am deeply grateful to a number of individuals whose support and guidance have been invaluable throughout the course of my undergraduate studies.

First and foremost, my heartfelt thanks go to my parents. Their unwavering support and constant encouragement have been the cornerstones of my journey. Their belief in my abilities and their sage advice have been instrumental in helping me navigate the challenges of my academic and personal life. I owe a significant part of my achievements to their sacrifices and profound influence.

I would also like to express my profound gratitude to Dr. Sabieh Anwar for providing me with the opportunity to undertake this research. His mentorship was pivotal in shaping the direction and success of this work. His trust in my capabilities and his guidance have been greatly appreciated and have enriched my learning experience.

Additionally, I extend my thanks to all my friends who have been part of this journey. The camaraderie and support I have found in them have made my educational experience both enjoyable and enriching. The moments we shared and the challenges we overcame together have added immense value to my time at the university.

I must also acknowledge the faculty of the Physics Department. Being a part of this department has been a remarkable experience. The lectures, discussions, and academic rigor provided by the professors have not only enhanced my knowledge but also fueled my passion for physics.

Thank you all for your support, without which this thesis would not have been possible.

# Contents

<b>1</b>	<b>Introduction</b>	<b>1</b>
<b>2</b>	<b>Motivation</b>	<b>4</b>
2.1	Quantum Imaging . . . . .	4
2.2	Experimental Preliminaries . . . . .	6
2.2.1	Spontaneous Parametric Down Conversion . . . . .	8
2.2.2	Quantum Nature of Light . . . . .	10
2.2.3	Freedman’s Test . . . . .	14
2.2.4	CHSH test . . . . .	17
<b>3</b>	<b>Approach</b>	<b>21</b>
3.1	Experimental Setup Design . . . . .	22
3.2	Utilization of Masks . . . . .	24
3.3	Mathematical Formulation for Setup . . . . .	28
3.4	Phase Extraction . . . . .	29
<b>4</b>	<b>Simulation of Amplitude and Phase Extraction</b>	<b>32</b>
4.1	Implementation . . . . .	32
4.1.1	Code Overview . . . . .	34
4.2	Results . . . . .	36
4.2.1	Bypassing the Masks: A Test of Quantum Phenomena . . . . .	38

5 Conclusion	42
Bibliography	44

# List of Figures

2.1	Setup employed to check the alignment of the BBO crystal. . . . .	9
2.2	Photodetection counts of detector A, B and the coincidence counts of AB, respectively. This is with the BBO crystal misaligned. . . . .	10
2.3	Photodetection counts of detector A, B and the coincidence counts of AB, respectively. The BBO has now been aligned. . . . .	11
2.4	Setup to check for the particle nature of light. The black filled box is our laser. A, B, and B' are bucket detectors. We make use of two half-wave plates. The polarizing beam splitter is used to send half the photons to detector B and the other half to B'. . . . .	12
2.5	Experimentally found quantum $g^{(2)}(0)$ and the ideal case of classical $g^{(2)}(0)$ . . . . .	14
2.6	Four detector setup for conducting the Freedman's test. . . . .	16
3.1	A panda made with black and white pixels. . . . .	21
3.2	Setup to create a ghost image [4]. After the respective beams pass through the object and mask SLMs, they are detected by the bucket detectors. Through these, coincidences are recorded and processed and we thus have a final reconstruction of the object as a ghost image. . .	24
4.1	Original amplitude of the object matrix. . . . .	37

4.2	Original amplitude of the object matrix. The color of the pixel represents its phase. . . . .	38
4.3	Extracted phase and amplitudes. . . . .	39
4.4	The object intended for reconstruction. . . . .	40
4.5	Resultant plot following the mask arm bypass, highlighting the absence of detectable image features. . . . .	40



# Chapter 1

## Introduction

Quantum imaging, a significant development in quantum mechanics, leverages the principles of quantum entanglement to surpass the limitations of classical imaging techniques. This field has recently emerged as a prominent topic within the photonics community, primarily due to its potential to revolutionize imaging technology through unique quantum properties.

Quantum imaging exploits phenomena such as entanglement, superposition, and precise quantum state measurements to achieve imaging results unattainable by classical methods. By utilizing entangled photon pairs and coincidence counting—produced via spontaneous parametric down-conversion—quantum imaging can reproduce classical imaging effects in a non-local manner. A notable technique within this realm is ghost imaging. In ghost imaging, two entangled light beams are employed: one beam illuminates the object but does not reach the detector directly, while the other, entangled beam, which never interacts with the object, is measured by a detector. The image is constructed by correlating the measurements from both beams.

Ghost imaging presents several advantages over classical imaging methods. Firstly, it

offers a higher signal-to-noise ratio (SNR) because the two-photon entangled beam is more robust against classical forms of attenuation [4]. Additionally, ghost imaging is highly effective in low-light conditions where classical imaging techniques struggle. Finally, when applied to larger systems, ghost imaging provides enhanced security. Intercepting the quantum states used in imaging disrupts the information, making any eavesdropping attempts detectable [2].

A significant objective in ghost imaging is the design of experimental setups and simulations to reconstruct images. However, a notable challenge is the inefficiency in imaging speed, which depends on the number of measurements required for image reconstruction. This parameter scales quadratically with the desired resolution, making high-resolution imaging time-consuming.

This thesis aims to redesign previous ghost imaging experiments [4], [3] using a simpler and more cost-effective approach. The goal is to demonstrate quantum entanglement and quantum imaging while maintaining high experimental accuracy. Our method reduces costs by employing a bucket avalanche photodiode (APD) detector instead of a more expensive single-photon detector or camera. This approach is not only cost-effective but also practical for educational and experimental purposes. However, before talking about the design of the experiment, there are preliminary experiments that have been conducted in the lab to ensure we have the artillery to take on this endeavor.

To address these challenges and validate our approach, we have conducted extensive simulations to model the experiments. These simulations serve multiple purposes: they help refine the experimental setup, predict outcomes, and validate the mathematical formulations underlying our methods. By comparing the simulated results with experimental data, we aim to ensure the robustness and accuracy of our approach. These

simulations are crucial for identifying potential issues and optimizing the parameters before actual laboratory implementation.

Future work will involve introducing noise into the system and recreating the experiment in the laboratory. This will necessitate addressing various experimental details such as acquisition times, post-processing of counts, and other procedural nuances. By advancing the techniques and methodologies in quantum imaging, this research aims to contribute to the broader understanding and practical applications of quantum mechanics in imaging technologies. Through innovation and simplification, we hope to make significant strides in both the theoretical and experimental aspects of quantum imaging.

# Chapter 2

## Motivation

### 2.1 Quantum Imaging

Quantum imaging represents a significant advancement in the field of imaging technologies, driven by its unique advantages over classical methods. This section delves into the in-depth motivations behind the pursuit and development of quantum imaging techniques.

The imaging techniques utilize the properties of quantum entanglement and superposition to achieve superior sensitivity and resolution compared to classical imaging methods. Entangled photons can detect finer details and subtle variations that are otherwise invisible with traditional techniques. This enhanced capability is particularly valuable in medical imaging and microscopy, where precision and detail are critical for accurate diagnoses and observations.

Quantum imaging inherently offers a higher signal-to-noise ratio (SNR) compared to classical imaging methods. The use of entangled photons reduces the impact of noise and other interferences, resulting in clearer and more accurate images. This

improved SNR is crucial in applications that require high precision, such as metrology and spectroscopy, where the detection of weak signals is essential.

Current research in quantum imaging is focused on addressing existing challenges, such as improving imaging speed and resolution. Efforts are being made to develop new algorithms and experimental setups to enhance the efficiency and accuracy of quantum imaging systems. The integration of machine learning techniques is also being explored to optimize image reconstruction and reduce computational complexity. Additionally, researchers are investigating the potential applications of quantum imaging in new domains, such as environmental monitoring and industrial inspection, leveraging its unique properties to achieve unprecedented levels of detail and accuracy.

Ghost imaging as well as quantum holography does not require the photons that interact with the object to be directly detected. Instead, correlations between distinct spatial light fields are used to generate the image, allowing for imaging in scenarios where classical methods would fail. This approach also reduces the effects of aberrations and distortions that are common in classical imaging, leading to more accurate reconstructions.

Ghost imaging is an unconventional method of capturing images that relies on the correlations between two distinct spatial light fields to generate an object's image. This process involves utilizing photons that have not directly interacted with the object. Each individual light field alone does not provide any image information about the object. However, by examining the correlations between these fields, it becomes possible to reconstruct an image. Originally demonstrated as a quantum entanglement phenomenon and linked to spontaneous parametric down-conversion (SPDC), ghost imaging has more recently been observed with entanglement swapped photons and

symmetry-engineered quantum states [6].

## 2.2 Experimental Preliminaries

We start with some rather fundamental experiments to investigate the more basic quantum properties of light, such as its particle nature and the ability of photon pairs to get entangled and exhibit non-local realism [1].

The experimental equipment includes all the necessary components to be able to perform the the experiments. Firstly, the pump laser used for all the experiments is a 405 nm violet laser. To create entangled pairs of photons, we have the spontaneous down-conversion unit. This consists of two BBO crystals stacked orthogonally on top of each other. This stacking configuration enables one of the BBO crystals to down-convert vertically polarized photons  $|V\rangle$ , while the other crystal down-converts horizontally polarized photons  $|H\rangle$ . The two photons produced are both 810 nm. Moreover, there are half-wave plates and quarter-wave plates to control and change the polarization of the incoming photons. The half-wave plate (HWP) is used to rotate linearly polarized light depending on the rotation angle that it is set at. As we vary the angle, the output polarization changes with respect to the polarization of the incoming beam of photons. The operation of the HWP can be represented by the matrix:

$$\hat{\mathbf{O}}_{HWP} = \begin{bmatrix} \cos(2\theta) & \sin(2\theta) \\ \sin(2\theta) & -\cos(2\theta) \end{bmatrix} \quad (2.1)$$

where  $\theta$  represents the angle that the HWP is rotated at.

If a photon with an initial polarization of  $H$  is fed into the HWP rotated at  $45^\circ$ ,

then it will emerge as a photon in the state  $V$ , as we can infer from the matrix (2.1). Similarly, when a photon initially in the state  $H$  passes through the HWP rotated to  $22.5^\circ$ , then we have:

$$\psi = \hat{\mathbf{O}}_{\text{HWP}} H$$

$$\psi = \begin{bmatrix} \cos(2\theta) & \sin(2\theta) \\ \sin(2\theta) & -\cos(2\theta) \end{bmatrix} \begin{bmatrix} 1 \\ 0 \end{bmatrix}$$

$$\psi = \begin{bmatrix} \cos(45^\circ) \\ \sin(45^\circ) \end{bmatrix}$$

$$\psi = \begin{bmatrix} \frac{1}{\sqrt{2}} \\ \frac{1}{\sqrt{2}} \end{bmatrix}$$

$$\psi = \frac{1}{\sqrt{2}} \begin{bmatrix} 1 \\ 1 \end{bmatrix}$$

There will be two emergent photons, one in state  $H$  and the other in state  $V$ , each with a component of  $\frac{1}{\sqrt{2}}$ .

A polarizing beam splitter, which is used in the latter experiments, splits light into its two orthogonal polarization components. The beam splitter we use causes the horizontal and vertical components to emerge perpendicular to each other because of the two refractive indices of the material it is made of.

We also need photon detection units for which we use avalanche photodiodes (APDs). APDs operate based on the principle of the avalanche effect. When a photon strikes the semiconductor material of the APD, it generates an electron-hole pair. In APDs,

the electric field within the device is high enough that these carriers can gain sufficient kinetic energy to create additional electron-hole pairs through impact ionization. This multiplication process results in an avalanche of charge carriers, hence the name. These generate an electric signal each time a photon is received. The electric pulse is sent to the FPGA (Field Programmable Gate Array) so that it may be processed into counts in the computer.

Coincidence counting involves the simultaneous detection of two or more particles at separate detectors. In the realm of quantum mechanics or quantum optics experiments, an economical approach to coincidence counting is implemented using a Field-Programmable Gate Array (FPGA) with an internal clock set at 50 MHz. This configuration allows for an effective coincidence window of  $2 \times 10$  ns, offering an efficient and cost-effective solution for concurrently counting single and coincident photons across multiple photodetectors. Photons are deemed coincident if they reach different detectors within a specified time coincidence window, in our case, 10 ns. Notably, owing to the independence of the arrival sequence of pulses, the actual coincidence window is precisely twice the width of the pulses. In our specific setup, this window spans 10 ns.

### 2.2.1 Spontaneous Parametric Down Conversion

The first task is to ensure that the BBO crystals are aligned properly to be able to down-convert both horizontally and vertically polarized photons. A half-wave plate (HWP) can rotate the linear polarization of an incoming beam. At a specific angle  $\theta$  (the angle between the incident beam's polarization and the HWP's optical axis), the HWP can convert a vertically polarized photon  $|V\rangle$  into a horizontally polarized photon  $|H\rangle$  and vice versa. Thus, if a vertically polarized beam  $|V\rangle$  passes through an HWP and the HWP is rotated through various  $\theta$  angles, at certain angles, the



polarization will switch from  $|V\rangle \rightarrow |H\rangle$ . If this converted beam then encounters a hypothetically misaligned BBO crystal that does not accept  $|H\rangle$  photons while the HWP is rotating, the horizontally polarized photons  $|H\rangle$  will not undergo down-conversion. Consequently, for some HWP orientations, there would be a reduction in the number of down-converted photons detected due to the misaligned crystal. Conversely, in a perfectly aligned BBO stack, both  $|H\rangle$  and  $|V\rangle$  polarized photons of the pump beam would be down-converted, resulting in no dips in the single-photon counts for an aligned BBO stack.

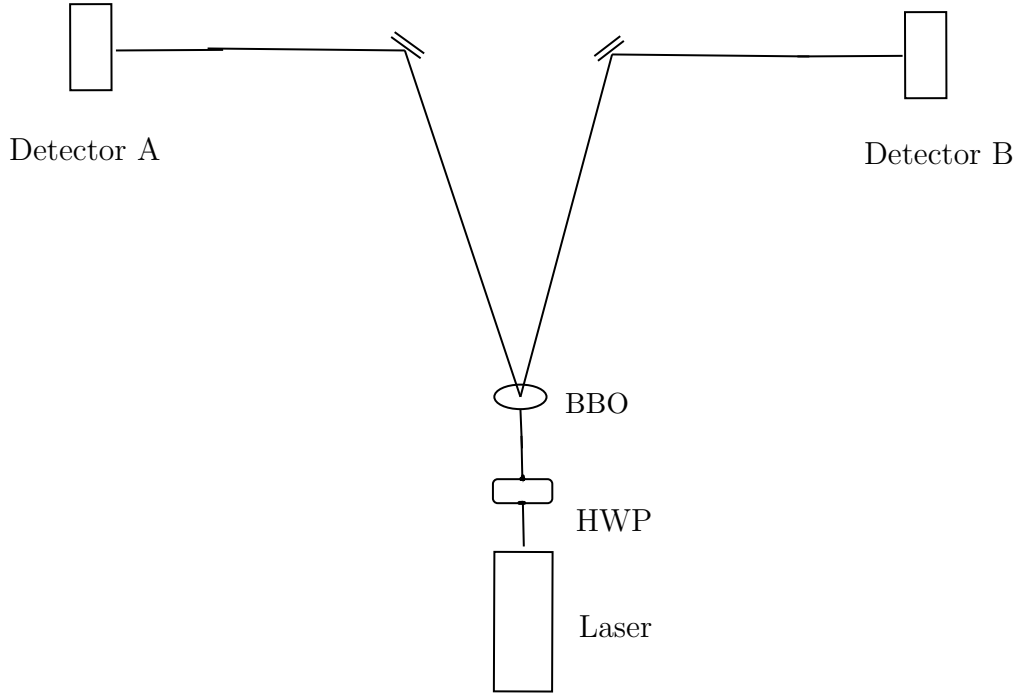


Figure 2.1: Setup employed to check the alignment of the BBO crystal.

To investigate this experimentally, the setup in figure 2.1 is used. As we can see in the plots in figure 2.2, there are dips in the counts in both detectors A and B, as well as the coincidence counts as the HWP rotates. This is what we expect when the BBO is misaligned. There are some photons that have not been downconverted.

When the BBO is aligned, we expect that there would be no dips in neither the

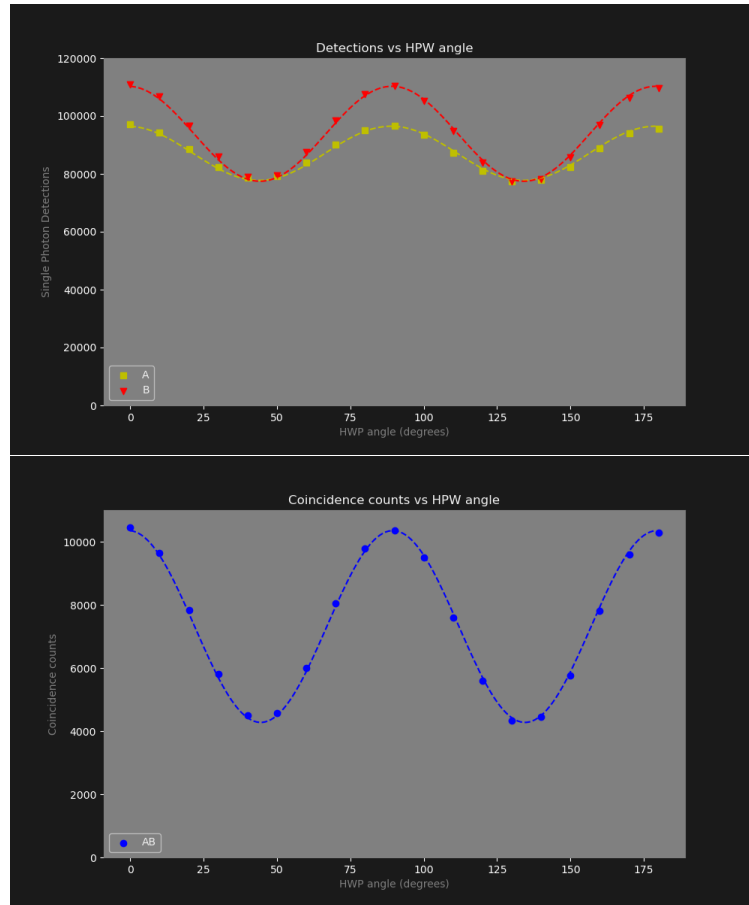


Figure 2.2: Photodetection counts of detector A, B and the coincidence counts of AB, respectively. This is with the BBO crystal misaligned.

coincidences not the individual detector counts. This can be confirmed as shown in figure 2.3

### 2.2.2 Quantum Nature of Light

To check for the quantum nature of light, we employ the setup in Figure 2.4. To carry out fine alignment of the detectors, the tilt of the detectors is adjusted using the rotating knobs of the mounts until both the individual and coincidence counts are maximized.

Once we have successfully controlled the polarization of light and completed the down-conversion of photons, the next critical step involves validating the photonic behavior

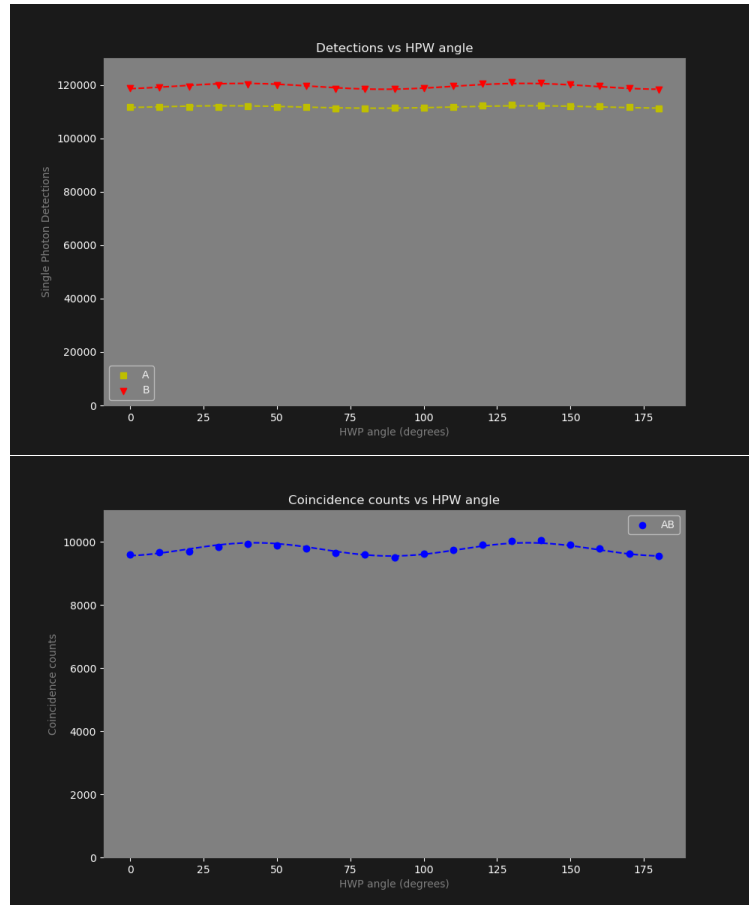


Figure 2.3: Photodetection counts of detector A, B and the coincidence counts of AB, respectively. The BBO has now been aligned.

of light. To achieve this, we incorporate a polarizing beam splitter (PBS) into the experimental setup, positioned approximately 3-4 inches from detector B. It is crucial to ensure that the PBS is oriented perpendicularly to the incoming photon beam. The PBS serves the purpose of splitting the beam into two components: a horizontally polarized reflected ray and a vertically polarized transmitted ray. Subsequently, one of these rays is directed into detector B, while the other is routed to detector B'. To further manipulate the polarization state and gather insightful data, an additional half-wave plate (HWP) is introduced between the BBO crystal and detector B. This configuration allows us to fine-tune the polarization characteristics of the incoming photons.

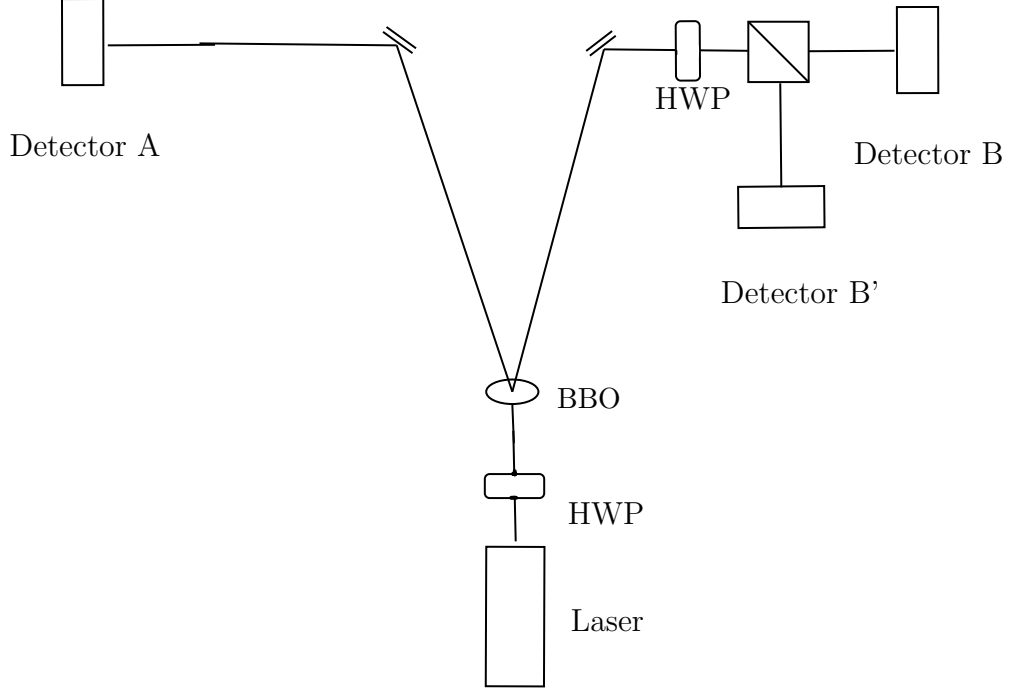


Figure 2.4: Setup to check for the particle nature of light. The black filled box is our laser. A, B, and B' are bucket detectors. We make use of two half-wave plates. The polarizing beam splitter is used to send half the photons to detector B and the other half to B'.

Throughout the experimentation process, counts from detectors A, B, and B', as well as the coincidence counts AB, AB', BB', and ABB', are recorded. To be able to demonstrate the quantum nature of light, the angle of the second HWP is systematically adjusted at 5-degree intervals. The resulting counts registered by the detectors are stored to be processed further.

Upon completion of data collection, an in-depth analysis ensues, aiming to determine whether the observed light behavior aligns with quantum particle characteristics. This assessment is facilitated by evaluating the second-order correlation function  $g^{(2)}(0)$ . We have the following expression for  $g^{(2)}(0)$

$$g^{(2)}(0) = \frac{P_{ABB'}(0)}{P_{AB}(0)P_{AB'}(0)} \quad (2.2)$$

The probabilities can be easily acquired using conditional probability to give the following

$$P_{AB}(0) = \frac{N_{AB}(0)}{N_A}$$

$$P_{AB'}(0) = \frac{N_{AB'}(0)}{N_A}$$

$$P_{ABB'}(0) = \frac{N_{ABB'}(0)}{N_A}$$

These can be plugged into (2.2) to give the final expression for the quantum coherence factor

$$g^{(2)}(0) = \frac{N_A N_{ABB'}}{N_{AB} N_{AB'}} \quad (2.3)$$

We must also consider the fact that there is a statistical error associated with having a finite time window, however small it may be. What is meant by this is that since we have a detection time window of 10 ns, if 2 photons have a time difference of detection that is less than 10 ns, the processor will count them as being coincident, even if they are not. They are statistically determined and the corresponding coherence factor due to accidental counts is also retrieved.

- Probability of accidental coincidence:

$$P'_{ABB'} = P_{AB} N_{B'} \Delta t + P_{AB'} N_B \Delta t$$

- $g^{(2)}(0)$  due to accidental counts:

$$g'^{(2)}(0) = N_A \Delta t \left( \frac{N_{B'}}{N_{AB'}} + \frac{N_B}{N_{AB}} \right)$$

The  $g^{(2)}(0)$  must come out to be around 0 to prove that we have observed the 'grainy-ness' of the light beam. Upon calculation, we can confirm that it does, as shown in figure 2.5.

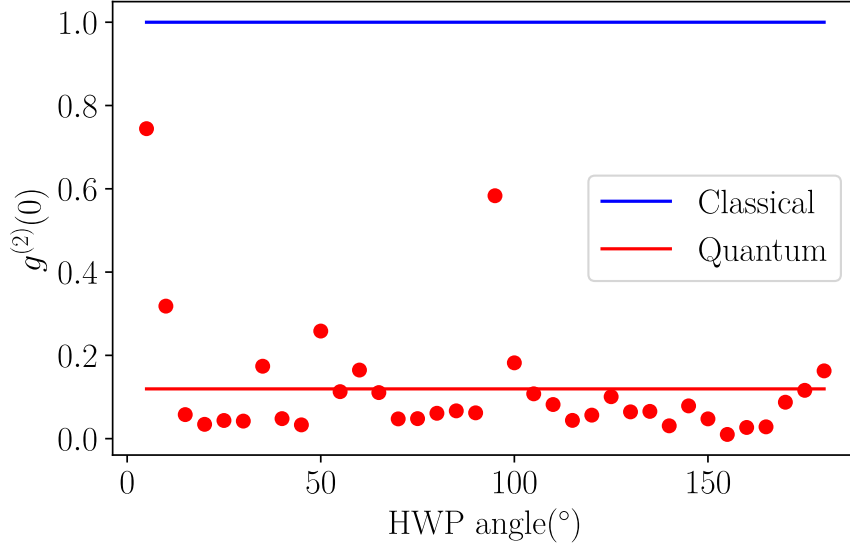


Figure 2.5: Experimentally found quantum  $g^{(2)}(0)$  and the ideal case of classical  $g^{(2)}(0)$ .

With that confirmed we must then move on to prove that the states of the photons outgoing from the BBO are entangled. For this, there are three tests to confirm non-localism: Freedman's test, Hardy's test, and CHSH test.

### 2.2.3 Freedman's Test

The first experiment investigating quantum entanglement and nonlocality was Freedman's test. The parameter used in this test was the quantity  $\delta$  defined by equation (2.4):

$$\delta = \frac{N(22.5^\circ) - N(67.5^\circ)}{N_0} - \frac{1}{4} \quad (2.4)$$

where  $N(\phi)$  represents the coincidence counts when the relative angle between the

two effective polarizer combinations is  $\phi$ , and  $N_0$  represents the coincidence counts recorded with no effective polarizer components present in both channels/beams. The parameter  $\delta$  was chosen because it allows us to determine whether local realism is obeyed or violated. By examining equation (2.4), we can infer that  $\delta$  can be directly determined from the coincidence counts data. Therefore, equation (2.4) will be used to determine the experimental value of  $\delta$ ,  $\delta_{\text{exp}}$ .

The quantum mechanical prediction for the quantity  $\delta$  is defined as:

$$\delta = \frac{\epsilon_A \epsilon_B}{2\sqrt{2}} - \frac{1}{4}, \quad (3.6)$$

where  $\epsilon_A$  and  $\epsilon_B$  represent the transmittance of the polarizers present in channel A and channel B, respectively.

Assuming locality, realism, and hidden variable arguments are obeyed,  $\delta$  attains a value  $\leq 0$ . This inequality is referred to as Freedman's inequality and places a constraint on the values of  $\delta$  if local realism is to be upheld:

$$\delta \leq 0 \quad (2.5)$$

Thus, when performing our experiment, we must obtain a value greater than 0.

For the Freedman's test, we wish to create the state  $\Phi^+$ , which is one of the Bell states (maximally entangled). To generate the state  $\Phi^+$ , the four-detector arrangement shown in Figure 2.6 was used. To obtain the state  $\Phi^+$ , we need the coefficients  $A$  and  $B$  in the equation

$$|\psi\rangle = A|HH\rangle + Be^{i\varphi}|VV\rangle \quad (2.6)$$

to be  $\frac{1}{\sqrt{2}}$  and the phase  $\varphi$  to be 0.

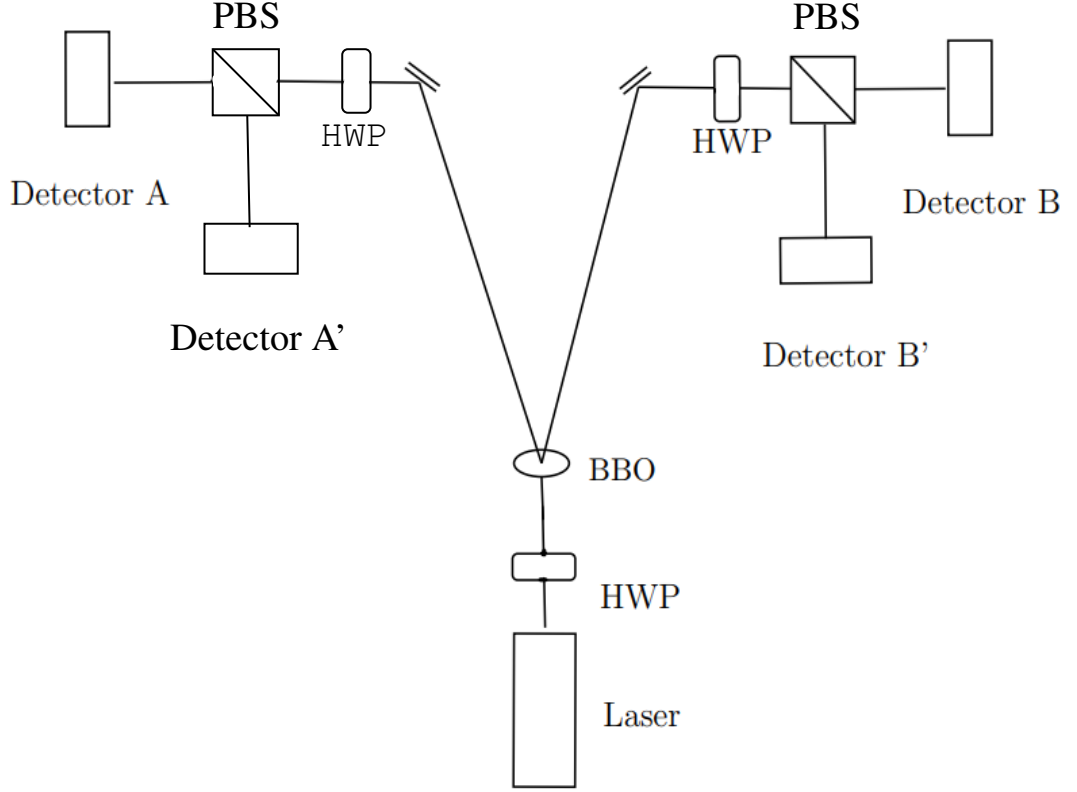


Figure 2.6: Four detector setup for conducting the Freedman's test.

To achieve the first condition, effective polarizers A and B are set at  $0^\circ$  to observe the  $|HH\rangle$  counts (A'B' counts). The pump beam HWP is then adjusted such that the AB coincidence counts, when setting the effective polarizers at  $90^\circ$  (which, in our setup, corresponds to setting the channel HWPs to half the required angle, i.e.,  $45^\circ$ ), and A'B' counts are approximately equal. It is ensured that for cross-orientations of the effective polarizers (one polarizer set at  $0^\circ$  and the other at  $90^\circ$ , and vice versa), we get minimum AB coincidence counts.

With these steps undertaken, the  $|HH\rangle$  and  $|VV\rangle$  counts in the  $\{|H\rangle, |V\rangle\}$  basis are approximately equalized ( $\approx 1:1$  ratio), and the  $|HV\rangle$  and  $|VH\rangle$  counts are minimized. In the SPDC setup depicted in Figure 2.1, a two-detector arrangement was used. However, entanglement experiments and the determination of transmittances necessitate



a four-detector configuration. After performing measurements and calculations, we obtain the following values for  $\epsilon_A$  and  $\epsilon_B$ :

$$\epsilon_A = 1.702 \pm 0.008$$

$$\epsilon_B = 1.661 \pm 0.007$$

Using these values, we calculate a  $\delta$  value of

$$\delta = 0.46384 \pm 0.00123$$

Since this value obeys our constraint of  $\delta > 0$ , we can safely say our hypothesis is proven: the states are entangled and exhibit non-local behavior.

### 2.2.4 CHSH test

The next key experiment is used to confirm entanglement and is the CHSH test, aiming to scrutinize the adherence or violation of local realism. The testing parameter under consideration was the quantity denoted as  $S$ , as defined in equation 2.7:

$$S = E(a, b) - E(a, b') + E(a', b) + E(a', b'), \quad (2.7)$$

where  $E(x, y)$  represents the expected outcome of a local realistic measurement for the analysis angle of  $x$  in channel A (signal) and  $y$  in channel B (idler), as specified in equation 2.8:

$$E(x, y) = \cos(2(x - y)). \quad (2.8)$$

The CHSH inequality is then expressed as  $|S| \leq 2$  under the assumptions of locality, reality, and hidden variable arguments.

Violation of this inequality, with  $|S| > 2$ , contradicts the predictions of local realism and implies non-local behavior. For an entangled state, such as  $\Phi^+$ , the theoretical value of  $S$  is  $S_{\text{th}} = 2\sqrt{2}$ . This theoretical value establishes the upper limit of the CHSH inequality under the assumption of non-locality.

Given experimental constraints, precisely generating the maximally entangled state  $\Phi^+$  can be challenging. Therefore, the experimental determination of  $S$  is expected to lie within the range defined by the following equation:

$$2 < S_{\text{exp}} < 2\sqrt{2}. \quad (2.9)$$

This range encapsulates the conditions for a successful violation of the CHSH inequality, providing evidence of non-locality in accordance with quantum mechanics. The analysis involves calculating the theoretical value of  $S$  for the specified analysis angles ( $a = -45^\circ$ ,  $a' = 0^\circ$ ,  $b = 22.5^\circ$ ,  $b' = -22.5^\circ$ ) and comparing it with the experimentally determined value, emphasizing the importance of achieving results beyond the classical bounds imposed by local realism.

The setup for the experiment the same as the one we used in the Freedman's test (figure 2.6). We must now achieve maximal violation of CHSH identity. To establish the Bell state, it is imperative to balance the counts for AB and A'B' while minimizing A'B and AB' counts in both the  $\{|H, V\rangle, |V, H\rangle\}$  and  $\{|D, A\rangle, |A, D\rangle\}$  bases. Minimizing A'B and AB' counts in both bases implies setting  $\phi$  to zero.

Firstly, we construct the  $\{|HV\rangle, |VH\rangle\}$  measurement basis. The HWP angles for A and B are set to  $0^\circ$ . In this configuration, the A and B detectors record horizontally polarized photons emitted by the source, and the A' and B' detectors register vertically polarized photons. The pump beam HWP is adjusted until the AB and A'B' coincidences are maximized, maintaining a ratio close to 1:1, while ensuring that A'B

and AB' coincidences are minimized.

Subsequently, the measurement basis is switched to  $\{|DA\rangle, |AD\rangle\}$  by setting the HWP angles for A and B to  $22.5^\circ$ , and the tilt of the quartz plate is adjusted to minimize the A'B and AB' coincidences. The AB and A'B' coincidences should remain maximized and approximately equal in number.

To refine the state further, a few iterations of the aforementioned steps are performed. Ultimately, when the AB and A'B' coincidences are approximately in a 1:1 ratio, and A'B and AB' coincidences are minimized in both measurement bases, the down-converted photons are generated in the desired Bell state.

After data has been collected, it is utilized to ascertain the probabilities referenced in equation 2.8. These probabilities, in turn, facilitate the determination of  $E(a, b)$ ,  $E(a, b')$ ,  $E(a', b)$ , and  $E(a', b')$ . The values for each of these expectation values comes out to be:

$$E(a, b) = 0.554 \pm 0.001$$

$$E(a, b') = -0.577 \pm 0.001$$

$$E(a', b) = 0.607 \pm 0.001$$

$$E(a', b') = 0.678 \pm 0.001$$

Once  $E(x, y)$  had been established for each set of analysis angle pairs, equation 2.7 enables the calculation of the experimental value of  $S$ , denoted as  $S_{\text{exp}}$ . Our value of  $S_{\text{exp}}$  comes out to be:

$$S_{\text{exp}} = 2.514 \pm 0.002$$

which agrees well with what we had expected. This confirmation attests that the

photon pairs in question were entangled and demonstrated a violation of local realism. This is evident as the CHSH inequality 2.9 has been breached by our observed value of  $S_{\text{exp}}$ .

# Chapter 3

## Approach

Now we must move on to actually figuring out the setup to reconstruct the ghost image. There are some necessary arrangements to be made to be able to achieve a fully reconstructed ghost image. What we want to do is to image a 2D object made of pixels. An example of something we could image is the panda shown in figure 3.1.



Figure 3.1: A panda made with black and white pixels.

Let us first go over what we know from the previous chapter. A photon source, in our case a laser beam being sent through a BBO crystal, is used to generate entangled photon pairs through a process called spontaneous parametric down-conversion (SPDC). An 405 nm wavelength photon is split into two lower-energy (810 nm) entangled

photons. In SPDC, a single photon is incident on the non-linear crystal, and it can split into two entangled photons.

After the entangled photons are produced, they are sent in different directions. One photon (called the signal photon) is sent to the object or scene being imaged, for which we use a spatial light modulator (SLM) to add amplitude change to the photon beam as a representation of the object. The other photon (called the idler photon) is directed towards an SLM that adds a series of random masks to the idler photon and then sends this 'masked' photon to the detector. The signal photon interacts with the object, and its properties are changed based on this interaction.

### 3.1 Experimental Setup Design

A spatial light modulator (SLM) is a device that can manipulate the properties of light, such as its phase, amplitude, or polarization, in a spatially varying manner. This means that different regions of the light beam can be controlled independently, allowing for precise manipulation of the light's characteristics. They can be thought of as a matrix or a pixel array of tiny polarizers, that control how much light is passing through each pixel and at what phase the incoming photon leaves. Each pixel on the SLM surface can be individually controlled to modify the phase, amplitude, polarization, or intensity of the incident light. After passing through the pixel array and undergoing modulation, the light exits the SLM with the desired spatial characteristics determined by the pixel control settings. Depending on the type of SLM, this mechanism can vary and may involve liquid crystals, micro-electromechanical systems (MEMS), deformable mirrors, or other technologies.

Our system for spatially resolving detection is implemented through the utilization of

an SLM, where a sequence of random binary patterns, known as masks, is displayed. The masks are randomly generated pixel settings on the SLM. Subsequently, the projection formed by these masks is captured by a bucket detector. The measured correlations offer insights into the similarity or overlap between the object and each applied mask. The process involves scanning through a series of these masks, and the duration of this scanning operation scales with the necessary resolution for the imaging task at hand. The spatial light modulator plays a crucial role in dynamically adapting the patterns, contributing to the versatility of the system in capturing detailed spatial information. This methodology provides a mechanism for extracting meaningful data about the object. The idler photon, which does not interact with the object, serves as a reference. The idler and signal photon beams are detected by a bucket detector. The correlation between the detected idler photons and the signal photons that interacted with the object is then analyzed. This correlation is a crucial quantum feature and is typically established through a coincidence measurement.

Despite the fact that the idler photons alone do not carry detailed spatial information, the correlations between the signal and idler photons can be used to reconstruct an image of the object. This is achieved through computational algorithms that exploit the quantum correlations to extract the spatial information. The resolution of the reconstructed image is determined by the number of pixels on the SLM as well as the number of masks used [5]. However, one limitation is the inefficient imaging speed, as the number of measurements needed for reconstruction scales quadratically with the required resolution (i.e. we are putting more masks in front of the beam to extract more information and therefore have a higher number of computations performed). The experimental setup needed to be able to reconstruct the image is as in figure 3.2. To proceed further, we require an en-depth explanation of what masks are, why we used them, and how they are implemented.

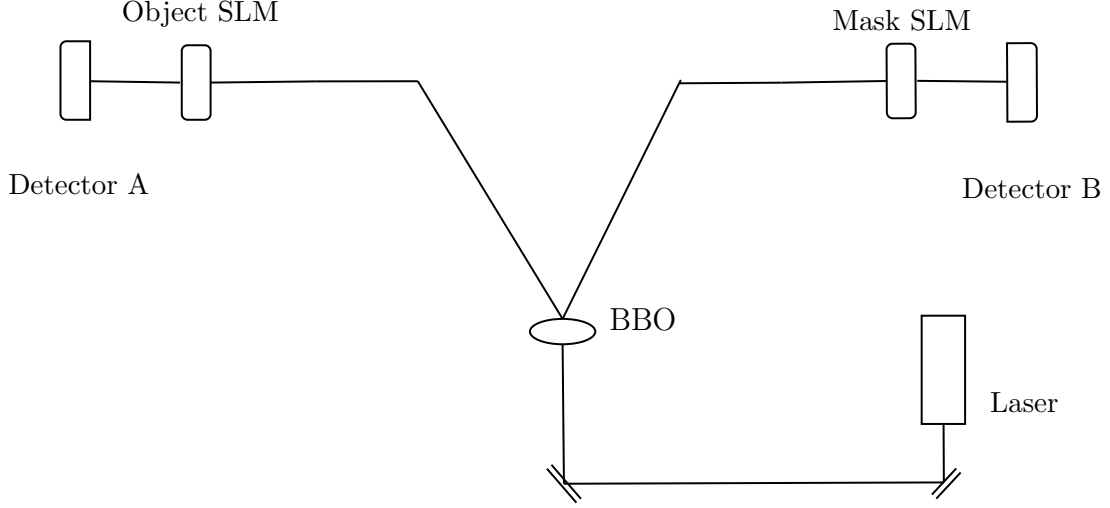


Figure 3.2: Setup to create a ghost image [4]. After the respective beams pass through the object and mask SLMs, they are detected by the bucket detectors. Through these, coincidences are recorded and processed and we thus have a final reconstruction of the object as a ghost image.

## 3.2 Utilization of Masks

In ghost imaging, masks are critical for modulating the incident light that illuminates the object. Each mask, or spatial light modulator, selectively allows portions of the light to pass while blocking others, thereby generating varied light patterns denoted by  $I_r(x, y)$ . These patterns are essential for effectively sampling the entire field of the object.

The output signal of the bucket detectors,  $B_r$ , initially presented in continuous form, needs discretization for practical digital implementation:

$$B_r = \sum_{p=1}^N \sum_{q=1}^N I_{ijpq} T_{pq}, \quad (3.1)$$

where  $I_{ijpq}$  represents the light intensity for the  $r$ -th pattern at pixel  $(p, q)$ , and  $T_{pq}$  denotes the pixel's transmittance. This sum aggregates the transmitted light over all pixels, collected by a bucket detector which captures all the transmitted or reflected



light without resolving the image [4].

Convolution plays a significant role in analyzing how the masks influence the detected signal. In mathematical terms, the interaction between the mask patterns and the object's transmittance function can be expressed through convolution:

$$B_r = (I_r * T)(u, v), \quad (3.2)$$

where  $*$  denotes convolution, and  $(u, v)$  are the spatial coordinates. This operation helps understand the overlap and interaction of the modulated light with the object's features, essential for reconstructing the image.

The number of masks (or patterns) used directly influences the image resolution and quality. An increase in the number of patterns ( $n = N^2$ ) enhances both resolution and quality by providing a more thorough sampling of the object's transmission characteristics. However, this increase also escalates computational demands and processing times. Optimal balance based on application-specific requirements is crucial.

Masks in ghost imaging are essential for controlled light modulation, enabling effective capture of an object's light transmission properties. The convolution concept further aids in mathematically modeling and improving the interaction between light patterns and the object, fundamental for advancing the image reconstruction process in ghost imaging.

## Error Analysis in Ghost Imaging

Error analysis is crucial in ghost imaging to ensure the reliability and accuracy of the reconstructed images. Several factors contribute to the errors in ghost imaging setups,

and understanding these is essential for optimizing system performance.

## **Photon Statistics and Shot Noise**

One of the primary sources of error in ghost imaging is related to photon statistics and shot noise. Shot noise, inherent in any detection process involving photons, arises due to the discrete nature of light and the random arrival of photons at the detector. This noise can be particularly significant in low-light conditions, which are common in high-resolution ghost imaging setups. To mitigate shot noise, increasing the light intensity or the integration time of the detector can be effective. However, care must be taken to avoid saturation of the detector and to manage increased light exposure, which might be detrimental in sensitive applications.

## **Ambient Light Interference**

Ambient light can significantly interfere with the detection process, introducing additional noise that can obscure the signal associated with the object's transmittance. To reduce this type of error, ghost imaging experiments are typically conducted in controlled environments where ambient light is minimized. Additionally, using narrow-band filters that match the spectral characteristics of the illumination source can help in rejecting out-of-band light, thus enhancing the signal-to-noise ratio.

## **Alignment Errors**

Misalignment between the light source, masks, and detectors can lead to significant errors in ghost imaging. Misalignment affects the spatial correlation between the mask patterns and the detected light, potentially leading to blurred or distorted images. Ensuring precise alignment through mechanical stabilization and using real-time alignment feedback systems can mitigate these errors. Calibration procedures should

be regularly performed to maintain alignment accuracy throughout the experiment.

## **Mask Imperfections**

The quality and design of the masks used in ghost imaging directly affect the quality of the resulting image. Imperfections in mask fabrication, such as non-uniformities or incorrect pattern generation, can lead to errors in the modulation of the light field and consequently in the image reconstruction process. Using high-quality, precision-manufactured masks and regularly verifying their integrity can help reduce these issues. Additionally, computational correction techniques can be employed to compensate for known mask imperfections.

## **Detector Sensitivity and Non-linearity**

The sensitivity and linearity of the bucket detector are critical in accurately measuring the total light intensity transmitted through the object. Detector non-linearity, where the response of the detector does not linearly correlate with the photon flux, can introduce errors in the intensity measurements, affecting the reconstructed image. Using detectors with a well-characterized linear response and calibrating them for the specific light levels used in experiments can reduce these errors.

## **Software and Computational Errors**

Errors in the software used for image reconstruction, such as bugs in the code or improper handling of data, can also affect the quality of the reconstructed image. Rigorous testing of the software, validation of the algorithms, and cross-verification with analytical solutions or experimental controls are necessary to ensure that computational errors are minimized.

### 3.3 Mathematical Formulation for Setup

In this section, we develop a mathematically rigorous framework for a ghost imaging system using a set of random masks and a simple  $3 \times 3$  matrix object. The objective is to demonstrate how the original object matrix  $O$  can be reconstructed from the convolution of  $O$  with multiple random masks.

Consider an object represented by a  $3 \times 3$  matrix  $O$ , where each element  $o_{ij}$  in  $O$  corresponds to the transmittance of the object at position  $(i, j)$ . We define nine  $3 \times 3$  random masks  $M_k$  (where  $k = 1, 2, \dots, 9$ ) used to modulate the light incident on the object. Each mask  $M_k$  consists of elements  $m_{kij}$  where  $m_{kij}$  can be either 0 or 1, indicating the blocking or passing of light at each pixel position.

The imaging system captures the light transmitted through the object as modulated by each mask. The convolution of the object matrix  $O$  with each mask matrix  $M_k$  results in an output matrix  $S_k$ , which is given by:

$$S_k = M_k * O \quad (3.3)$$

where  $*$  denotes the convolution operation. For a  $3 \times 3$  matrix using discrete convolution, the  $(i, j)$ -th element of  $S_k$  is computed as:

$$s_{kij} = \sum_{a=-1}^1 \sum_{b=-1}^1 m_{k,i+a,j+b} \cdot o_{i-a,j-b} \quad (3.4)$$

assuming zero-padding outside the boundaries of  $O$ .

To reconstruct the object matrix  $O$  from the output matrices  $S_k$ , we assume linear independence of the mask patterns and sufficient coverage of the object's features

across all masks. The reconstruction can be approached by solving a set of linear equations derived from the output matrices  $S_k$ , aiming to best approximate the original matrix  $O$ . We set up the reconstruction problem as follows:

$$\min_{\hat{O}} \left\| \sum_{k=1}^9 M_k * \hat{O} - S_k \right\|^2 \quad (3.5)$$

where  $\hat{O}$  is the estimate of the original object matrix  $O$ , and the norm represents the sum of squared differences between the convolved estimate and the measured output matrices.

The above formulation requires numerical methods such as iterative algorithms or optimization routines to solve. By iteratively adjusting  $\hat{O}$ , minimizing the reconstruction error, the original object matrix  $O$  can be effectively recovered. The success of this method depends on the randomness and diversity of the masks  $M_k$ , which should collectively sample all parts of the object space sufficiently.

This mathematical formulation provides a framework for implementing ghost imaging in a controlled, simulated environment, demonstrating the principles of image reconstruction using convolution and matrix operations.

### 3.4 Phase Extraction

Quantum holography represents a significant advancement over traditional imaging methods by allowing the extraction of both amplitude and phase information without directly detecting the photons that have interacted with the object. As can be noted, this is just taking the idea of ghost imaging a step further. This method utilizes the phenomenon of induced coherence without induced emission, as demonstrated in the

nonlinear interferometer setup.

In the setup described by Töpfer et al. [7], two beams—object and reference—are generated via spontaneous parametric down-conversion (SPDC) in a nonlinear SU(1,1) interferometer. The object beam interacts with the sample and carries information about its phase and amplitude, encoded in the transmission function  $\tau(x, y) = t(x, y)e^{i\theta(x, y)}$ , where  $t(x, y)$  and  $\theta(x, y)$  represent the amplitude and phase of the object beam, respectively.

To extract the phase information, the technique of phase-shifting holography is employed. This involves recording a series of holograms with varying global phase shifts introduced via the interferometer's adjustable parameters. By setting these phase shifts at  $0$ ,  $\pi/2$ ,  $\pi$ , and  $3\pi/2$ , and processing the resultant images, the phase  $\theta(x, y)$  at each pixel can be determined from the interference patterns.

The intensity of the light in each recorded hologram can be described by the equation:

$$N\Delta\phi(x, y) \sim 1 + t(x, y) \cos[\theta(x, y) - \nu(x, y) + \Delta\phi], \quad (3.6)$$

where  $\Delta\phi$  represents the phase shift, and  $\nu(x, y)$  is the phase alteration caused by the nonlinear processes within the interferometer.

From the recorded images under different phase shifts, the phase  $\theta(x, y)$  at each pixel is calculated using the equation:

$$\theta(x, y) = \arctan \left( \frac{N_{3\pi/2}(x, y) - N_{\pi/2}(x, y)}{N_0(x, y) - N_\pi(x, y)} \right), \quad (3.7)$$

and the amplitude  $t(x, y)$  is given by:

$$t(x, y) = 2 \times \sqrt{\left(N_{3\pi/2}(x, y) - N_{\pi/2}(x, y)\right)^2 + \left(N_0(x, y) - N_\pi(x, y)\right)^2}. \quad (3.8)$$

Implementing this approach requires precise control over the phase shifts and a high degree of coherence between the interfering beams, which can be done using the two SLMs. The phase and amplitude extracted from the holograms provide a detailed map of the object's optical properties, which is essential for applications such as biomedical imaging, where detailed structural information is necessary.

# Chapter 4

## Simulation of Amplitude and Phase Extraction

In this chapter, we discuss the implementation of a simulation designed to demonstrate the extraction of amplitude and phase information from a modeled ghost imaging setup. The simulation utilizes a set of randomly generated binary masks and a randomly generated amplitude matrix representing the object. The objective is to reconstruct the object's amplitude and phase information through computational methods, mirroring the principles discussed in the quantum holography section.

### 4.1 Implementation

The Python programming language, renowned for its simplicity and powerful libraries, was chosen for this simulation. The code employs libraries such as NumPy for matrix operations and Matplotlib for visualization, which are well-suited for numerical and graphical tasks respectively.

The script initiates by importing necessary libraries and defining the dimensions of a complex object matrix, where the real part represents the amplitude and the imaginary



part encodes the phase of the light at each pixel. It then proceeds to generate a random amplitude matrix for the object and several binary masks. Binary masks are applied to modulate this complex matrix, simulating the modulation of light as it interacts with the object. Phase information is extracted from the measurements, simulating the phase recovery process typical in quantum holography. The simulation mimics the process of applying these masks in a ghost imaging setup and calculates the reconstructed amplitude and phase of the object matrix.

The object in the simulation is conceptualized as a set of pixels on a Spatial Light Modulator (SLM), where each pixel can either transmit or reflect light. This is modeled mathematically in the object matrix  $O$ :

- Each element  $o_{ij}$  in the object matrix represents a pixel's ability to transmit light, with 1 indicating full transmittance (completely transparent) and 0 representing full reflectance (completely opaque).
- Intermediate values between 0 and 1 denote the fraction of light transmitted through each pixel, allowing for the creation of grayscale images that vary in brightness and contrast.

This representation is critical for simulating how different parts of the object interact differently with the incident light, influencing the resultant imaging data recorded after the light passes through the masks.

The primary functions of the script include:

- **Complex Object Matrix Generation:** Generates a complex matrix where each element is a complex number formed by random amplitude and phase values, representing the light's characteristics at each pixel.
- **Binary Mask Application:** Applies a series of randomly generated binary masks to the complex object matrix.

- **Measurement Simulation:** Calculates the total light transmitted through each mask, resulting in a series of complex measurements from which phase information can be derived.
- **Phase Extraction:** Extracts the phase from each measurement, demonstrating how phase information can be retrieved in a practical imaging setup.

Below is a simplified version of the code that is used to conduct the simulations.

#### 4.1.1 Code Overview

Listing 4.1: Python script for simulating amplitude and phase extraction in ghost imaging.

---

```
import numpy as np
import matplotlib.pyplot as plt

def generatematrix(rows, cols):
    amplitude = np.random.rand(rows, cols)
    phase = np.random.rand(rows, cols) * 2 * np.pi
    return amplitude * np.exp(1j * phase)

def generatemasks(rows, cols, num_masks):
    return [np.random.randint(2, size=(rows, cols)) for _ in
            range(num_masks)]

def apply_masks(object_matrix, masks):
    return [np.sum(mask * object_matrix) for mask in masks]

def extract_phase(measurements):
    return np.angle(measurements)
```

```

# Parameters

rows, cols = 12, 12

num_masks = 9

# Generate object matrix and masks

O = generatematrix(rows, cols)

masks = generatemasks(rows, cols, num_masks)

# Apply masks and simulate measurement

measurements = apply_masks(O, masks)

# Extract phases

extracted_phases = extract_phase(measurements)

```

---

The object matrix  $O$  and the binary masks  $M_k$  play a significant role in ghost imaging:

- The object matrix  $O$  simulates the amplitude characteristics of the object, where each element  $o_{ij}$  in the matrix represents the amplitude of the object at position  $(i, j)$ .
- Each binary mask  $M_k$  modulates the light incident on the object. The mask matrix elements are binary, with 0 indicating light blockage and 1 allowing light passage, thus creating different light patterns on the object.

As mentioned in chapter 3, the mathematical formulation involves the convolution of the object matrix  $O$  with each mask  $M_k$ , expressed as:

$$S_k = M_k * O$$

where  $*$  denotes the convolution operation. The output  $S_k$  represents the light pattern

recorded after interaction with the mask and the object. Each element  $s_{kij}$  would ideally be computed through the convolution:

$$s_{kij} = \sum_{a=-1}^1 \sum_{b=-1}^1 m_{k,i+a,j+b} \cdot o_{i-a,j-b}$$

assuming boundary conditions like zero-padding.

This simulation framework provides a more realistic scenario for testing and demonstrating the capabilities of ghost imaging techniques, particularly in terms of handling complex light modulation and phase-sensitive measurements. It serves as a useful educational tool for understanding advanced imaging techniques.

## 4.2 Results

The simulation process outlined in the previous sections aimed to demonstrate the ability of our setup to accurately reconstruct both the amplitude and phase of a simulated object using phase-shifting holography. Here, we present and discuss the results obtained from the simulation, showcasing the effectiveness of the computational model and the phase extraction technique.

The simulation generated three key outputs:

- **Original Amplitude of the Object:** This image represents the amplitude values of the object matrix  $O$  before any processing. It provides a baseline for comparing the reconstructed amplitude.
- **Extracted Amplitude:** This image shows the amplitude reconstructed from the simulation data, derived using the equations provided in the phase-shifting holography method.

- **Extracted Phase:** Similarly, this image depicts the phase reconstructed from the simulation, offering a visualization of how well the phase information has been retrieved from the interference patterns.

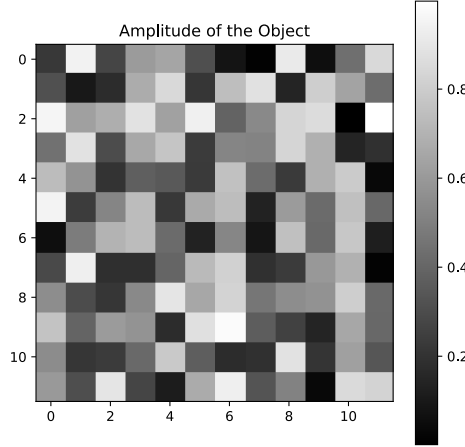


Figure 4.1: Original amplitude of the object matrix.

The comparison between the original and reconstructed images demonstrates the capability of the simulation to retrieve the amplitude and phase information with high fidelity.

The extracted amplitude closely matches the original amplitude of the object, as shown in the amplitude images. This indicates that our setup can accurately capture and reconstruct the amplitude details of the object, validating the amplitude extraction process implemented in the simulation.

The phase image effectively displays the spatial phase distribution of the object. The close correspondence between the reconstructed phase and the original phase of the object confirms that our simulation can effectively decode phase information from the interference patterns generated during the holographic process.

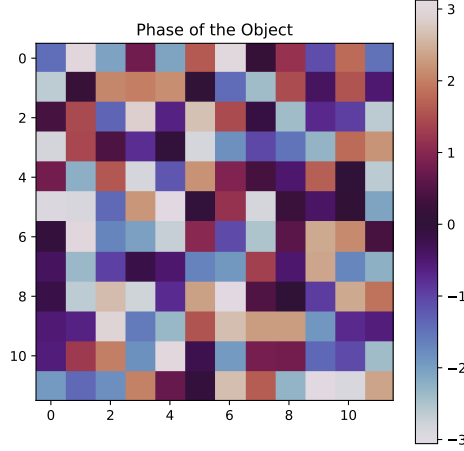


Figure 4.2: Original amplitude of the object matrix. The color of the pixel represents its phase.

The results of the simulation are visually represented in figures 4.1, 4.2, and 4.3.

These figures illustrate the effectiveness of the simulation in reproducing the object's properties and underline the accuracy of the phase-shifting holography technique used in our setup.

The results affirm that the simulated setup is capable of accurately reconstructing both the amplitude and phase of the object from the simulated measurements. This successful validation highlights the potential of our computational approach in applications of holographic imaging and phase-sensitive measurements, setting a foundation for future research and development in quantum imaging technologies.

#### 4.2.1 Bypassing the Masks: A Test of Quantum Phenomena

To further validate the role of quantum phenomena in our imaging process, we conducted a critical test by effectively disabling the mask arm of our setup. This was

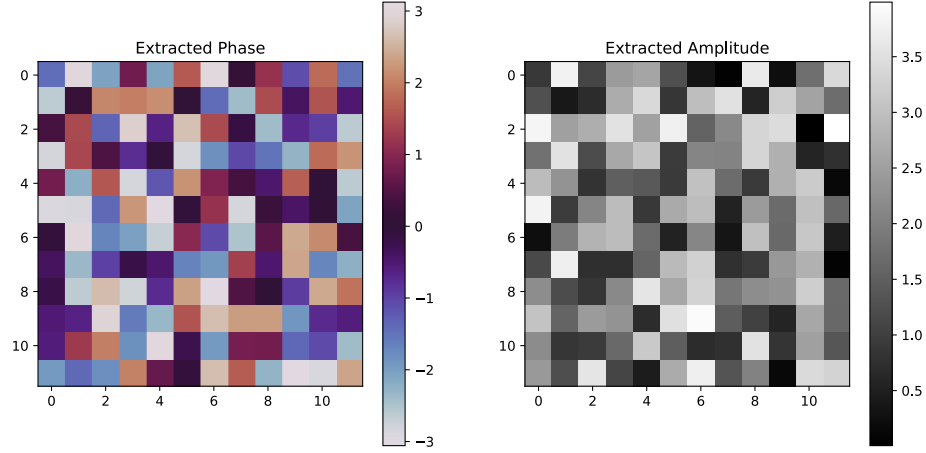


Figure 4.3: Extracted phase and amplitudes.

achieved by modifying each mask in the simulation to be a matrix entirely composed of zeros, thereby ensuring no light modulation occurs through these masks. The purpose of this experiment is to confirm whether the resultant imaging is strictly due to the quantum interference and not merely a byproduct of classical light patterns or unintended light leakage.

This test is designed to rigorously assess whether the reconstructed images we obtain are genuinely a consequence of the quantum interference properties harnessed in our setup, or if they might erroneously be derived from any residual classical light paths within the system. By setting all elements of the mask matrix to zero, we simulate a scenario where no light should theoretically be transmitted through the mask pathway. Consequently, any resultant imaging would indicate a non-quantum mechanism at play.

The outcomes, as depicted in Figures 4.4 and 4.5, unequivocally demonstrate the absence of any visible image when the mask arm is bypassed. This confirms our hypothesis: the imaging results previously obtained are indeed attributable to quantum

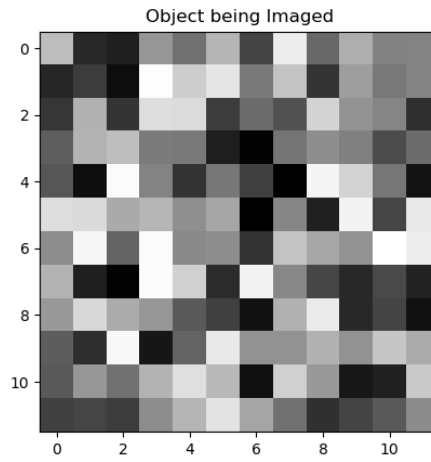


Figure 4.4: The object intended for reconstruction.

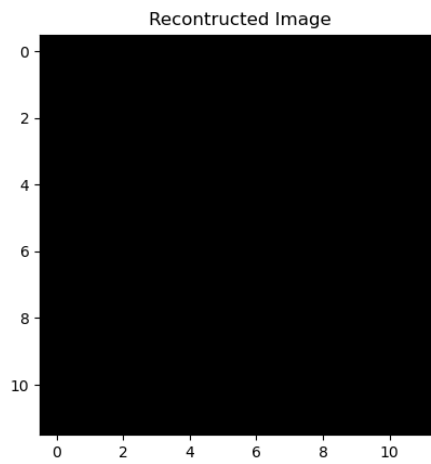


Figure 4.5: Resultant plot following the mask arm bypass, highlighting the absence of detectable image features.



phenomena. The lack of image formation in this test underscores the essential role that quantum interference plays in our experimental setup, and it substantiates the effectiveness of the quantum imaging techniques we are employing.

This finding not only reinforces the validity of our quantum imaging approach but also provides a robust methodological foundation for future experiments aimed at exploring and harnessing quantum phenomena for advanced imaging applications.

# Chapter 5

## Conclusion

The research presented in this thesis confirms the robust capabilities of quantum imaging techniques through comprehensive simulations and theoretical analysis. The implemented simulations effectively demonstrate the ability to reconstruct both amplitude and phase details of objects, showcasing the advanced potential of quantum holography and ghost imaging. Through the meticulous design of experiments and the strategic utilization of quantum properties such as entanglement and interference, this work provides significant insights into overcoming traditional imaging barriers.

A critical part of the study was to validate the quantum nature of the imaging process. The experiments designed to bypass the mask arm conclusively demonstrated that the imaging results were not artifacts of classical light patterns but were genuinely derived from quantum phenomena. This validation not only strengthens the reliability of quantum imaging techniques but also opens up new avenues for secure and precise imaging applications.

Future work will focus on refining these techniques and exploring their applicability in real-world scenarios. This includes enhancing the efficiency of image reconstruction,

reducing computational demands, and integrating these methods into practical imaging devices. The potential for quantum imaging to revolutionize fields such as biomedical imaging, security, and remote sensing is immense, and ongoing advancements in quantum technologies will further facilitate these developments.

In conclusion, this thesis not only demonstrates the practical implementation of quantum imaging techniques but also sets the stage for future innovations in the field. The successful simulation and validation of these techniques mark a significant step forward in the application of quantum mechanics to imaging technologies, promising to elevate the standards of imaging precision and security and quantum photonics experiments.

# Bibliography

- [1] Sabieh Anwar. *Quantum Mechanics in the Single Photon Laboratory*, pages 4–1–5–26. IOP Publishing, 2020.
- [2] M D’Angelo and Y H Shih. Quantum imaging. *Laser Physics Letters*, 2(12):567, sep 2005. doi: 10.1002/lapl.200510054. URL <https://dx.doi.org/10.1002/lapl.200510054>.
- [3] Hugo Defienne, Bienvenu Ndagano, Ashley Lyons, and Daniele Faccio. Polarization entanglement-enabled quantum holography. *Nature Physics*, 17(5):591–597, 2021. ISSN 1745-2481. doi: 10.1038/s41567-020-01156-1. URL <https://doi.org/10.1038/s41567-020-01156-1>.
- [4] Chané Moodley and Andrew Forbes. Super-resolved quantum ghost imaging. *Scientific Reports*, 12(1):10346, 2022. ISSN 2045-2322. doi: 10.1038/s41598-022-14648-2. URL <https://doi.org/10.1038/s41598-022-14648-2>.
- [5] Kyuki Shibuya, Katsuhiro Nakae, Yasuhiro Mizutani, and Tetsuo Iwata. Comparison of reconstructed images between ghost imaging and hadamard transform imaging. *Optical Review*, 22(6):897–902, 12 2015. ISSN 1349-9432. doi: 10.1007/s10043-015-0138-x. URL <https://doi.org/10.1007/s10043-015-0138-x>.
- [6] Yanhua Shih. Quantum imaging. *IEEE Journal of Selected Topics in Quantum Electronics*, 13(4):1016–1030, 2007. doi: 10.1109/JSTQE.2007.902724.

- [7] Sebastian Töpfer, Marta Gilaberte Basset, Jorge Fuenzalida, Fabian Steinlechner, Juan P. Torres, and Markus Gräfe. Quantum holography with undetected light. *Science Advances*, 8(2), January 2022. ISSN 2375-2548. doi: 10.1126/sciadv.abl4301. URL <http://dx.doi.org/10.1126/sciadv.abl4301>.